

# Substrate recognition by norovirus polymerase: microsecond molecular dynamics study

Kamil Maláč · Ivan Barvík

Received: 7 October 2012 / Accepted: 18 April 2013 / Published online: 26 April 2013  
© Springer Science+Business Media Dordrecht 2013

**Abstract** Molecular dynamics simulations of complexes between Norwalk virus RNA dependent RNA polymerase and its natural CTP and 2dCTP (both containing the O5′–C5′–C4′–O4′ sequence of atoms bridging the triphosphate and sugar moiety) or modified coCTP (C5′–O5′–C4′–O4′), cocCTP (C5′–O5′–C4′–C4′′) substrates were produced by means of CUDA programmable graphical processing units and the ACEMD software package. It enabled us to gain microsecond MD trajectories clearly showing that similar nucleoside triphosphates can bind surprisingly differently into the active site of the Norwalk virus RNA dependent RNA polymerase. It corresponds to their different modes of action (CTP—substrate, 2dCTP—poor substrate, coCTP—chain terminator, cocCTP—inhibitor). Moreover, extremely rare events—as repetitive pervasion of Arg182 into a potentially reaction promoting arrangement—were captured.

**Keywords** Norwalk virus · Hepatitis C virus · RNA dependent RNA polymerase · Molecular dynamics · Phosphonate · Competitive inhibitor · Chain terminator · NAMD · GPU · CUDA · ACEMD

## Introduction

Some viruses containing just the RNA genome are reproduced in host cells by RNA dependent RNA polymerase (RdRp) [1, 2]. Norwalk virus (NV) is a major cause of gastroenteritis outbreaks in developed countries [3, 4]. Unfortunately, effective treatments are not currently available. Hepatitis C virus (HCV) is spread among 3 %, or 170 million, of world population, of which only about 25 % are having symptoms [2]. Current treatment with interferon- $\alpha$  (immunomodulation) and ribavirin (nucleotide inhibitor) has limited efficiency and numerous side effects. Only 40–50 % of people exposed to HCV outbreak fully recover while rest is affected by chronic liver problems, with possibility of developing cirrhosis or even liver cancer [2]. Those patients undergoing interferon/ribavirin treatment also face the prospects of significant adverse effects that include fatigue, hemolytic anemia, depression, and flulike symptoms which ultimately lead to high rates of drug discontinuations [1].

In attempts to improve on the overall HCV cure rate and reduce or eliminate the serious side effects associated with interferon/ribavirin therapy, the search for direct acting antivirals (DAAs) that are safe and effective has become an urgent endeavor [1]. Recently, two protease inhibitors, telaprevir and boceprevir, in combination with interferon/ribavirin have been approved for treating HCV infection. However, they bring additional side effects that require further medical management [1]. Therefore, the search continues for novel agents with complementary mechanisms of action.

RdRp is not present in mammalian cells. Therefore, it is a suitable target for inhibition [5]. Mostly, the RdRp enzyme has four subunits. One of them has an active site for replication. The other three subunits help replicase to

**Electronic supplementary material** The online version of this article (doi:10.1007/s10822-013-9652-8) contains supplementary material, which is available to authorized users.

K. Maláč · I. Barvík (✉)  
Faculty of Mathematics and Physics, Institute of Physics,  
Charles University, Ke Karlovu 5, Prague 2 121 16,  
Czech Republic  
e-mail: ibarvik@karlov.mff.cuni.cz

locate and bind the 3' end of RNA. RdRps contain the classic structural domains, denoted fingers, palm, and thumb, of other single-chain polynucleotide polymerases [6] (Fig. S1). Crystal structure of NV RdRp reveals the carboxyl terminus in the active site cleft, which is reminiscent of the carboxyl-terminal extension domain and “plough” loop in bacteriophage  $\phi 6$  RdRp, as well as the carboxyl-terminal segment and  $\beta$ -loop insertion in the thumb domain of HCV RdRp [7]. RNA binding displaces the C-terminal tail from the active site cleft of NV RdRp. The binding of RNA also cause the central helix of the thumb domain (residues 435–449) to rotate by  $22^\circ$ , thus inducing the formation of a binding groove for the primer strand [3] (Fig. S2).

In contrast to most other single-chain polymerases of known structure, the finger and thumb domains are connected in the RdRps and are therefore not free to change conformation independently of each other [6]. The encircled active site structure makes it unlikely that major swinging motions of the fingers domain act to reposition the nascent base pair from an initial preinsertion site into the catalytic site, as is seen in other classes of single-subunit polymerases. Therefore, RdRps use a fully prepositioned templating base for nucleotide recognition [8] (Fig. S2).

Generally, nucleotide substrate binds to the polymerase-primer/template complex (step 1), and this complex isomerizes into a catalytically active complex (step 2). Phosphoryl transfer occurs (step 3), followed by a second conformational change (step 4) and pyrophosphate release (step 5) [9]. In HIV reverse transcriptase (HIV RT), step 2 involves an inward bending of fingertips toward the palm by about  $20^\circ$  resulting in a displacement of the outermost parts of the domain by more than  $5\text{\AA}$ . As a result, a number of residues are brought into contact with the incoming nucleoside triphosphate [10]. Closure of the fingers is also a noteworthy feature of dNTP binding in members of both the DNA polymerase I and terminal transferase families [10].

RdRps, in contrast, close their encircled active sites for catalysis using a subtle structural rearrangement in the palm domain. The key element of 3Dpol/NV active site closure is a subtle shift of motif A (depicted in Fig. 1d as a blue ribbon) to position the essential Asp233/Asp242 for metal binding and subsequent catalysis [3, 8].

One possibility of HCV treatment is non-nucleoside inhibition (NNI) of RdRp using allosteric inhibitors. They prevent HCV RdRp from reaching an active conformation [5]. In fact more than 80 crystal complexes of HCV RdRp

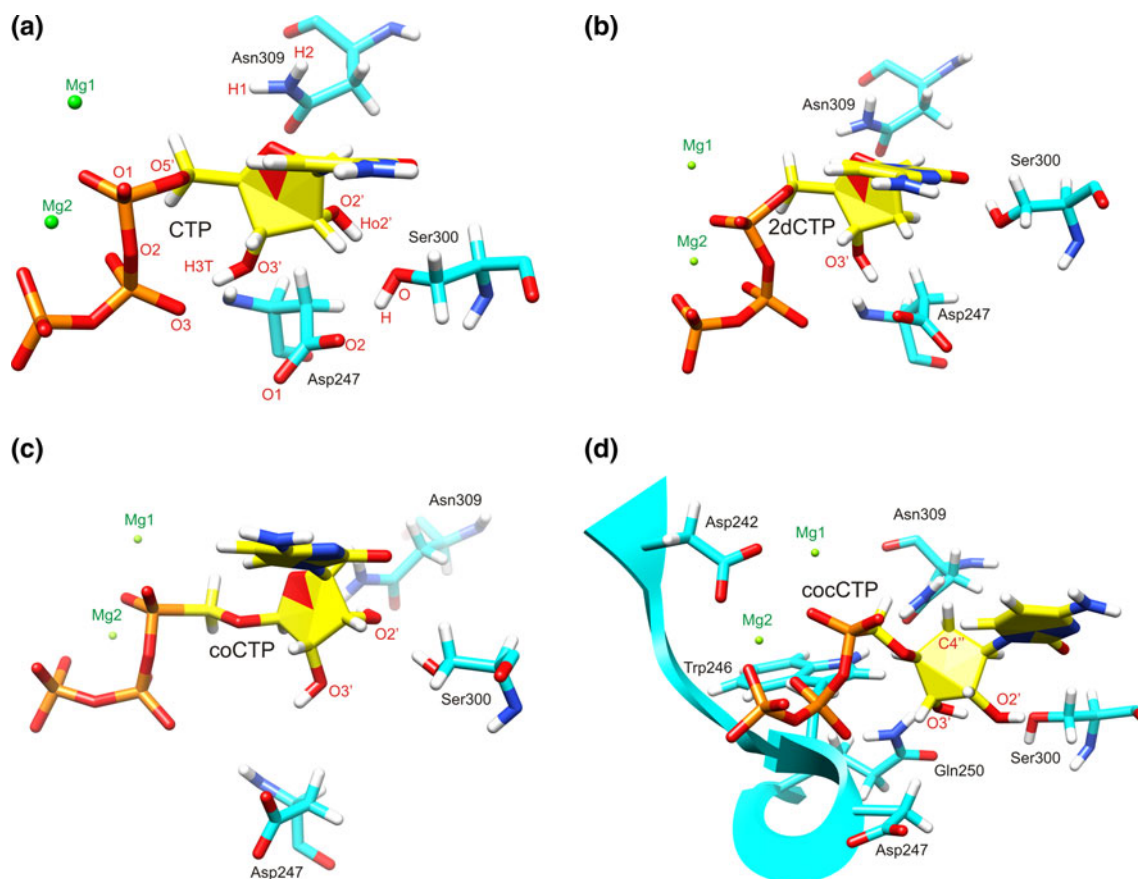


**Fig. 1** CTP, 2dCTP, coCTP and cocCTP in the NV RdRp active site

with small molecule allosteric inhibitors have been reported [1]. Several suitable binding sites for NNIs on the enzyme allow combination therapy. Inhibitors bind to the thumb cavity, which is crucial for “fingertip-thumb” interaction, thus forcing enzyme to remain in the inactive form [2]. Human clinical trials evaluating HCV NNIs as monotherapy have all shown viral breakthrough resulting from rapid emergence of resistant virus [1].

In contrast, nucleoside-based HCV RdRp inhibitors (nucleosides and nucleotide prodrugs—to enhance cellular uptake) have the potential to become the backbone of HCV therapeutic regimens. These nucleoside-based agents have demonstrated a high barrier to resistance. No other small molecule DAA developed to date has been able to mirror these characteristics [1]. This high barrier to resistance suggests that there is a high degree of amino acid conservation in the active site of HCV RdRp and that only subtle amino acid changes in the active site, which do not impair the replication fitness of the virus, are tolerated [1].

Nucleoside inhibitors of HCV RdRp have been explored in recent years [1, 5, 11–16]. They are converted by host cells into nucleotides, nucleoside diphosphates and nucleoside triphosphates. During the viral replication, they are incorporated into the synthesized RNA and act as chain terminators. In the case of HCV, 2'-C-methyl nucleosides are mostly used. They confer antiviral activity irrespectively to the base [11]. The methyl group added to C2' of ribose transforms a nucleotide substrate into a chain terminator. Several proof of concept clinical studies have shown that the combination of a nucleoside (2'- $\alpha$ -F-2'- $\beta$ -C-methylpyridine) with a HCV protease inhibitor and the combination of two nucleotide prodrugs (2'- $\alpha$ -F-2'- $\beta$ -C-methyluridine 5'-phosphoramidate and 3', 5'-cyclic phosphate prodrug of 2'- $\alpha$ -F-2'- $\beta$ -C-methylguanosine) have the potential to deliver an interferon/ribavirin free combination therapy [1]. Nevertheless, Bristol-Myers Squibb's disastrous phase 2 combination trial of the HCV drugs BMS-986094 and daclatasvir, which has caused the death of one patient and severe heart and kidney damage to another eight, has raised questions about this class of nucleoside inhibitors [16].

But there are other promising structural motives. Recent experimental studies show that (S)-9-[3-hydroxy-2-(phosphonomethoxy)propyl]-adenine (S-HPMPA—a substance known for more than 20 years) in a suitable prodrug form—might be able to fight HCV too [14]. Nucleosides and nucleotides are known to inhibit HCV during the elongation phase of viral RNA synthesis via a nonobligate chain termination mechanism. Dinucleotides have the potential to inhibit RNA replication at the initiation phase by behaving as primer molecules [1, 12, 13].

Molecular dynamics (MD) simulations are a well-established tool for the investigation of structural features of biomolecules at atomic detail level. Nucleotide

incorporation efficiency, fidelity and the catalytic mechanism of different polymerases were studied by means of MD simulations in past [17–24]. We used MD simulations to investigate binding of phosphoramidate dinucleotides toward HCV RdRp [12, 13].

CUDA programmable graphical processing units (GPUs) enable now to extend MD trajectories on time scales, which were until recently available only with supercomputing facilities. It inspired us to try to find subtle differences in binding of quite similar substrates into the active site of RdRp. Microsecond MD trajectories could provide time for sufficient relaxation of complexes and capturing of even very slow conformational changes.

A series of adenosine 5'-phosphonate analogues were designed in [15] to mimic naturally occurring adenosine monophosphate. These compounds were synthesized and evaluated in a cellular hepatitis C virus replication assay. To elucidate the mechanism of action of these novel adenosine phosphonates, their diphosphate derivatives were synthesized. Further nucleotide incorporation assays by HCV RdRp revealed that coATP (analogous to coCTP in Fig. S3) can serve as a chain terminator, whereas co-ATP (analogous to cocCTP in Fig. S3) compound is a competitive inhibitor.

Here, MD simulations of complexes between NV RdRp and its natural CTP and 2dCTP (both containing the O5'-C5'-C4'-O4' sequence of atoms bridging the triphosphate and sugar moiety—see Fig. S3) or modified coCTP (C5'-O5'-C4'-O4') and cocCTP (C5'-O5'-C4'-C4'') substrates were produced and analyzed in detail.

## Methodology

There is an apparent structural similarity of NV/HCV RdRps, which allows straightforward transferability of many observations. NV RdRp complexes with double helical nucleic acids and CTP appeared in literature recently (3BSN, 3BSO [3], 3H5X, 3H5Y [4]). The structures of the NV RdRp complexes provided the first high resolution views of RdRp complexes trapped immediately before nucleotidyl transfer. Indirect effects from crystal packing appear to have fortuitously trapped these complexes at this stage of reaction cycle. The distal end of the primer-template duplex is located near a symmetry-related polymerase molecule, and there is insufficient space for primer extension to occur in this crystal form. As a result, polymerase molecules in this crystal form bind substrates and assemble active complexes that can only proceed up to the point immediately prior to nucleotidyl transfer. Therefore, the geometry of the NV RdRp active site was determined very precisely in [3, 4] uncovering clearly a hydrogen bonding connecting the 2'-OH/3'-OH groups of the incoming NTP with Asp247, Ser300 and Asn309 of NV

RdRp (their counterparts in HCV RdRp are Asp225, Ser282 and Asn291).

Therefore, 3BSO [3] was chosen as a suitable representative of RdRps in our MD simulations. Simulated systems were surrounded by ~15565 TIP3P [25] water molecules which extended to a distance of approximately 10 Å (in each direction) from the RdRp atoms. This gives a periodic box size of ~84, ~90, ~73 Å. New \*.inpcrd (initial coordinates) and \*.prmtop (molecular topology, force field etc.) files for the whole simulated system including modified residues, were created by use of the TLEAP module (AMBER software package [26]).

The AMBER force field used in this study [27, 28] does not contain force constants needed to describe modified parts of the phosphonate analogs. The force field parameters were therefore completed with those obtained from ab initio calculations consistently with the original approach [27] (Figs. S4–S5). RESP charges were computed at the HF/6-31G\* level. Force constants were fitted to achieve the agreement of ~1 kcal/mol between QM (MP2/6-31G\*) and MM relative energies of different conformers of the CH<sub>3</sub>–O–PO<sub>2</sub>–CH<sub>2</sub>–O–CH<sub>3</sub> model system.

Almost half of the proteome of living organisms is constituted of metalloproteins. Unfortunately, the ability of the current generation of molecular dynamics pairwise-additive force fields to properly describe metal pockets is severely lacking due to the intrinsic difficulty of handling polarization and charge transfer contributions [29]. Magnesium ions are usually represented as atoms with a formal point charge +2 that interact with the protein environment and the substrate through non-bonded interactions. In binuclear active sites, however, high charges can lead to repulsion between two Mg<sup>2+</sup> and instabilities, resulting in an alteration of the proper coordination of the Mg<sup>2+</sup> ions by the ligands [24, 30, 31]. For example, using the standard AMBER Mg<sup>2+</sup> ions ( $R^* = 0.7926$  Å,  $\epsilon = 0.8947$ ), the coordination of both Mg(b) and Mg(c) in the  $\beta$ -polymerase active site changed [24]: Mg(b) lost contact with Asp192 and O2B (a non-bridging  $\beta$ -phosphate oxygen of the dNTP) and was instead coordinated by O3B (the oxygen bridging the  $\beta$  and  $\gamma$  phosphates of the dNTP); Mg(c) lost contact with the O3' of the primer and O1A (a non-bridging  $\alpha$ -phosphate oxygen of the dNTP coordinating both metal ions in the crystal structure).

Further, a general tendency to underestimate slightly magnesium-ligand distances, leading to a more compact active site, is usually observed in MD simulations [29, 32]. A consistent set of empirical interaction parameters for the alkali and alkaline-earth metal cations was derived by performing free energy perturbation simulations in aqueous solution [32]. The resulting parameters reproduce the observed hydration free energies as well as radial distribution functions of these ions. However, the value of radius

for Mg<sup>2+</sup> ions shows a less good agreement with the observed distance than for any of the other ions and appears to be slightly too small [32] ( $R^* = 0.7926$  used in the AMBER force-field). Even though using Mg<sup>2+</sup> with  $R^* = 1.300$  Å and  $\epsilon = 0.06$  yielded the best structural results among the traditional one-atom Mg<sup>2+</sup> models, there were some significant discrepancies between the crystal structures and the modeled structures, i.e. increased Mg(b)–Mg(c), O1A–Mg(b) distances [24].

The Aqvist-Warshel (AW) model that uses cationic dummy atoms and has proven very useful in accurately representing the energetics and structures of systems with transition metals such as octahedrally coordinated bivalent manganese ions and tetrahedrally coordinated bivalent zinc ions in mononuclear and binuclear metalloenzymes [24]. The AW model allow for stable coordination geometry by placing the cationic dummy atoms at the defined positions around the central metal atom and for a smaller repulsion between the metal ions in binuclear sites by distributing the positive charge over the cationic dummy atoms. Attaching cationic dummy atoms to the central metal atom at defined positions leads to more directed electrostatic interactions with ligands and delocalization of the charge to prevent repulsion in binuclear sites. In [24], the AW model always performed better than the best traditional one-atom Mg<sup>2+</sup> model. In particular, the Mg(b)–Mg(c) distance and the distance between Mg(b) and O1A of the incoming dNTP were much closer to the X-ray crystallographic distances. Further, in the case of the RNA ligase ribozyme [33], the Mg–O bond lengths obtained via a dummy approach [24] were more similar to those measured in QM/MM MD simulations and in the X-ray structures of other Mg<sup>2+</sup> containing enzymes. In the PDB database, magnesium ions are invariably hexacoordinated with octahedral geometry. An analysis of structures available in the PDB to the 2002 indicated that the Mg–O bond length can range between 2.05 and 2.25 Å [24].

Equilibration MD trajectories lasting for 5 ns were computed with the aid of the NAMD 2.7 software package [34]. The smooth Particle-mesh Ewald (PME) method was employed for long-range electrostatic forces [35]. The non-bonded cutoff was set to 9 Å. The SHAKE algorithm (tolerance 0.0005) was applied to constrain bonds where the hydrogen atoms were involved [36]. Simulated systems were energy minimized, then the Langevin dynamics was used for a temperature control [34]. The simulated systems were heated from 0 to 310 K. The Langevin piston method was applied to reach an efficient pressure control with target pressure set to 1 atm [34]. The integration timestep was set to 2 fs. A multiprocessor system equipped with 16 Intel Itanium CPUs was used for equilibration MD simulations.

For production runs (reaching up to 1,050 ns) we have used ACEMD v. 2591 [37, 38] running on a local workstation



equipped with Nvidia GPU. ACEMD is a new generation molecular dynamics software which runs exclusively on graphics processing units (GPUs) at the equivalent speed of tens to hundred of standard processors. ACEMD implements all features of an MD simulation on a CUDA-compatible GPU device, including those usually required for production simulations in the NVT ensemble (i.e. bonded and non-bonded force term computation, velocity-Verlet integration, Langevin thermostatic control, smooth Ewald long-range electrostatics (PME), and hydrogen bond constraints implemented using the M-shake algorithm and RATTLE for velocity constraints within the velocity Verlet integration scheme [39, 40]). ACEMD does not presently contain a barostat for production runs, so simulations in the NPT ensemble are not possible. However, it is noted that with large molecular systems, changes in volume due to the pressure control are very limited after an initial equilibration making NVT simulations viable for production runs [37, 38]. It was proven on multiple biomolecular systems including membrane proteins [41–43]. Therefore, our production runs have been performed in the NVT ensemble, Langevin thermostat at 310 K, computing the electrostatic interactions with the particle-mesh Ewalds algorithm. The non-bonded cutoff was set to 9 Å. Also implemented in ACEMD is the hydrogen mass repartitioning scheme (the mass of the bonded heavy atoms to hydrogen is repartitioned among hydrogen atoms, leaving the total mass of the system unchanged) used, for instance, in codes such as Gromacs, which allows an increased time step of up to 4 fs [37, 44]. Therefore, the integration timestep in our production MD runs was set to 3 fs. The total energy was conserved within MD simulations (Fig. S6). For production MD runs CUDA programmable NVIDIA GTX-580 graphical processing units (GPUs, equipped with 480 cores) were used.

Data were recorded every 75 ps. MD trajectories were analyzed with the aid of the CHIMERA 1.5.3, VMD 1.9, Curves+ and AMBER10/ptraj software packages [26, 45–47]. Figures were produced by means of the ICM Molsoft 3.7 software package.

## Results

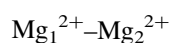
MD simulations of complexes consisting of NV RdRp and its natural (CTP, 2dCTP—Fig. S3) or modified (coCTP, cocCTP—Fig. S3) substrates were carried out. The closed active site of NV RdRp at the moment just before the phosphoryl transfer step was studied.

## RMSD

Structural instabilities could appear in MD simulations from many reasons. Generally, crystal structures are

affected by crystal packing forces. Therefore, remarkable conformational changes may accompany the process of relaxation. Further, the closed state of NV RdRp was established in crystals due to its interactions with CTP. Analogs of CTP used in this study could stimulate a transition of NV RdRp to the open state. Moreover, instabilities can simply arise due to artifacts or disbalances in contemporary force fields [28].

Therefore, the stability of simulated biomolecules was assessed by the root-mean-square deviation (RMSD). Time evolution of RMSD for NV RdRp as well as for nucleic acids is provided in Fig. S7. It clearly shows that all simulated systems were stable over microsecond MD simulations.



In MD simulations of binuclear active sites [24], remarkable instabilities due to the excessive repulsion arising between magnesium ions (represented as VdW spheres with non-polarizable point charges +2) were observed. The seven-point representation (with dummy atoms) of magnesium ions should prevent these instabilities [24], but according to the best of our knowledge, no one has verified whether it will remain true on a microsecond time scale. The time evolution of  $\text{Mg}_1^{2+}-\text{Mg}_2^{2+}$  and  $\text{Mg}_{1,2}^{2+}$ -ligand distances shows (Fig. S8) that stable NV RdRp active sites were gained here.

Moreover, no tendency of NV RdRp to move from close to open state was found here. It would have to start through erosion of contacts between  $\text{Mg}_2^{2+}$  and Asp242 from Motif A (Figs. 1d, S2).

Nevertheless, remarkable differences in recognition of the 2'OH group of CTP, coCTP and cocCTP by Asp247 (which is part of Motif A as well—Fig. 1d) were observed (see below). Its potential impacts on transitions of NV RdRp either from open to close or from close to open state will be the subject for further investigation.

## Structural analysis

Conformational preferences of CTP, 2dCTP, coCTP and cocCTP (Fig. S3) and their contacts with side chains of amino acids whose mutation significantly decreases the catalytic efficiency of RdRp were studied in detail here:

1. In past, one of us studied isosteric phosphonate linkages in the context of dinucleotides and oligonucleotides by means of ab initio calculations and MD simulations [48]. Large differences in conformational preferences of the torsion angles  $\text{O5}'-\text{C5}'-\text{C4}'-\text{O4}'$  and  $\text{C5}'-\text{O5}'-\text{C4}'-\text{O4}'$  were found (and confirmed by NMR [48]). It significantly influenced melting temperatures of whole double

helical structures. Interestingly, the same conformational preference (as observed for C5′–O5′–C4′–O4′ in [48]) was seen in the crystal structure of an isosteric phosphonate analogue GS-9148 bound in the active site of HIV RT (PDB id: 3kk1 [49]). Therefore, different conformational preferences of natural and modified NTPs (Fig. S3) were expected to appear here with serious implications on the geometry of the NV RdRp active site.

2. In poliovirus 3Dpol RdRp, incorporation of a 2′-deoxyribonucleotide with a correct base should occur at a frequency 1/7,500 [50]. Therefore, conformational preferences of sugars (sugar puckering) were quantified here using the pseudorotation angle.
3. In NV RdRp [3], the 2′-OH group of the incoming nucleoside triphosphate accepts a hydrogen bond from Asn309 and donates a hydrogen bond to Ser300, which in turn donates a hydrogen bond to Asp247. This pattern of hydrogen bonding shows how these highly conserved residues distinguish ribonucleotides from 2′-deoxyribonucleotides. Homologous residues in poliovirus 3Dpol RdRp are Asn297, Ser288, and Asp238 respectively. 3Dpol derivatives that contain alanine at position Asp238 or Asn297 are incapable of distinguishing between ATP and 2′-dATP. While the loss of the Asn297 side chain caused a 20-fold reduction in the observed rate constant for correct nucleotide incorporation, the loss of the Asp-238 side chain caused a 2,000-fold reduction [51]. Therefore, the 2′OH-Ser300–Asp247 mutual contacts were monitored here in detail (Fig. 1).
4. In NV RdRp X-ray structures [3], the CTP bases form hydrogen bonds with the complementary guanosine base of the template and stack against the 3′-terminal base of the primer, as well as the Arg182 guanidino group. Arg182 is near the NTP  $\alpha$ -phosphate. This arginine is highly conserved in RdRps. Arg158 is the homologous residue in HCV RdRp. In the presence of

**Fig. 3** CTP conformational preference and its interactions in the NV RdRp active site: **A01** CTP O5′–C5′–C4′–O4′ torsion angle; **A02** CTP Sugar Puckering; **A03** Intramolecular hydrogen bond: CTP\_3′OH– $\beta$ -phosphate\_CTP; **A04** Asp247–3′OH\_CTP; **A05** Asp247–Ser300; **A06** Ser300–2′OH\_CTP; **A07** Asp247–2′OH\_CTP; **A08** Arg182– $\alpha$ -phosphate\_CTP; **A09** Arg182– $\beta$ -phosphate\_CTP; **A10** Primer\_O3′– $\alpha$ -phosphate\_CTP

only  $Mg^{2+}$ , the HCV RdRp R158A mutant was severely affected for all activities: initiation of RNA synthesis by a de novo mechanism, extension from a primed template, non-templated nucleotide addition, and synthesis of a recombinant RNA product from two or more noncovalently linked templates (template switch) [52]. Arg residues occupy a similar position in distantly related enzymes like HIV RT. The HIV RT R72A has the *k<sub>cat</sub>* of the polymerase reaction reduced by nearly 100-fold with poly(rA) template [53]. In DNA polymerase  $\beta$ , Arg183 is found to form a salt bridge with the  $\beta$ -phosphate of an incoming NTP. A mutation of Arg183 to alanine significantly lowers the catalytic efficiency, which agrees well with the results from energy decomposition analysis, where the residues Arg183 (–7.1 kcal/mol) and Arg149 (–4.6 kcal/mol) were found to have the most significant contributions [20, 21]. The so-called arginine fingers play a crucial role in the GTP hydrolysis promoted by various GTPases [54–56]. The effect of Arg789 in Ras/GAP complexes is associated with its direct interaction with the transition state charge distribution [54]. Therefore, Arg182 contacts with triphosphate moieties of our NTPs were studied here in detail as well (Fig. 2).

5. The distance separating reaction substrates—i.e. the phosphorus atom of the  $\alpha$ -phosphate group of NTPs and the O3′-terminal atom of the RNA primer was followed here (Fig. S2b). However, the phosphate/phosphonate substitution in coCTP and cocCTP could affect the chemical step of the NV RdRp reaction. A direct comparison of the  $\alpha$ P–O3′ distances thus

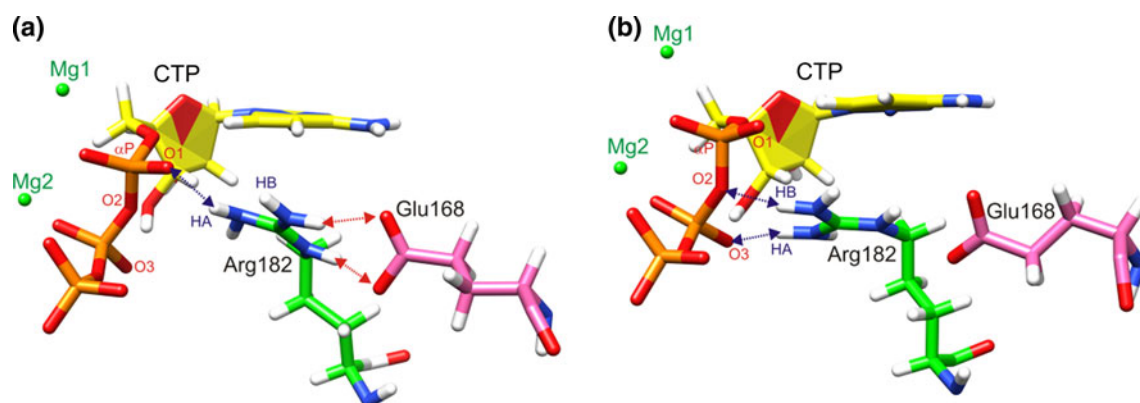
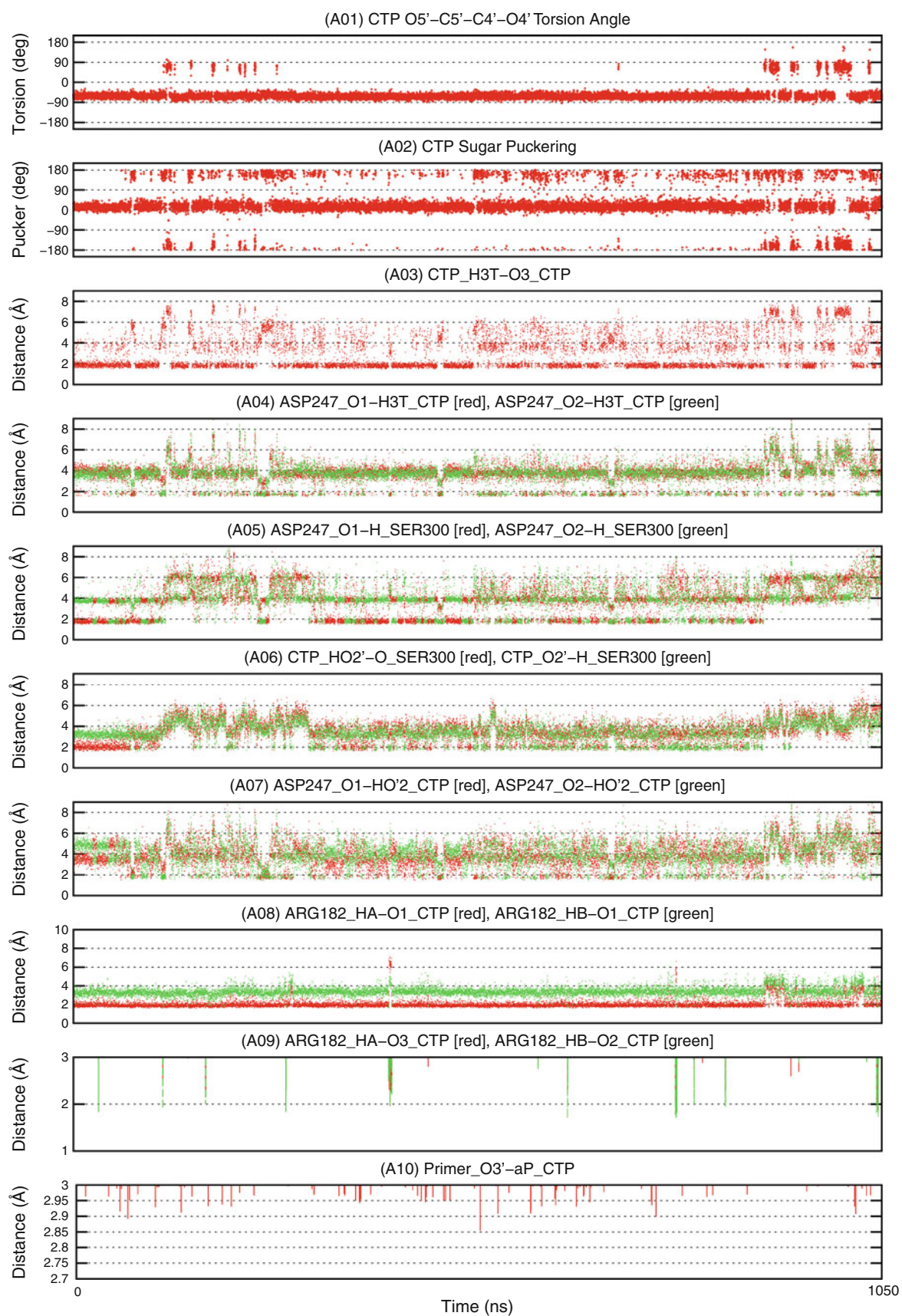


**Fig. 2** **a** Arg182 interacting with the  $\alpha$ -phosphate group of CTP; **b** Arg182 interacting with the  $\beta$ -phosphate group of CTP





probably makes sense especially in the case of closely related structures (CTP vs. 2dCTP) and (coCTP vs. cocCTP—where it could provide the most straightforward explanation of their different modes of action—competitive inhibition vs. chain termination).

### CTP: Figs. 1a, 2, 3—Graph A01–A10

CTP was mostly in the canonical A-RNA conformation within the MD simulation. The O5'–C5'–C4'–O4' torsion angle (Fig. S3) was in the **–gauche** conformation (Fig. 3—Graph A1) and the ribose moiety in the **C3'-endo** conformation (Fig. 3—Graph A2). Nevertheless, reversible short-living conformational transitions of the ribose moiety to **C2'-endo** were captured repeatedly within the microsecond MD trajectory. In moments, when contacts of CTP with amino acid side chains in the NV RdRp active site were temporarily disrupted (see below), the ribose passed even to **C3'-exo** and the O5'–C5'–C4'–O4' torsion angle was in **+gauche**.

For most of the time, the 2'OH group of CTP was hydrogen bonded with Asp247 (Fig. 3—Graph A7) and Ser300 (Fig. 3—Graph A6). Asp247 and Ser300 interacted with each other as well (Fig. 3—Graph A5). In fact, all possible combinations of hydrogen bond donors (group 2'OH/atom HO2'; Ser300/H—see Fig. 1a) and acceptors (group 2'OH/atom O2'; Asp247/O1, O2; Ser300/O—see Fig. 1a) were applied. Where necessary, green and red lines in charts distinguish multiple hydrogen bonds of the same amino acid side chain. In crystal structures [3], the 2'-OH group of CTP donates a hydrogen bond to Ser300, which in turn donates a hydrogen bond to Asp247. MD simulations thus show that the hydrogen bond network is much more dynamic in solution.

Arg182 (atom HA—Fig. 2a) was in close contacts with the non-bridging oxygen atom of the  $\alpha$ -phosphate group of CTP (atom O1—Fig. 2a) for most of the time (Fig. 3—Graph A8—red line). Arg182 was stabilized in this position by Glu168 (Fig. 2a). The polymerase reaction event would break the bond between the  $\alpha$ P and O2 atoms (Fig. 2a) that should move away each from other. Therefore, we speculate that Arg182 binding to the  $\alpha$ -phosphate group of CTP is more likely to hinder the reaction (of course—only future QM/MM calculations can be conclusive).

Nevertheless, about once every 100 ns, the Arg182 side chain lost any contacts with Glu168 and instead interacted with the  $\beta$ -phosphate group of CTP (atom O3—Fig. 2b) and with the oxygen atom bridging the  $\alpha$  and  $\beta$  phosphate groups of CTP (atom O2—Fig. 2b, Fig. 3—Graph A9). It means that Arg182 interacted exclusively with the pyrophosphate moiety of CTP. The role of analogous Arg72

from HIV RT in the pyrophosphate release was demonstrated experimentally [53]. Moreover, the latter configuration (Fig. 2b) seems to be optimal for lowering of the transition state energy, because Arg182 interacts directly with the oxygen atom of the scissile bond (atom O2—Fig. 2b). Nevertheless, only future QM/MM calculations can be conclusive.

The distance separating reaction substrates—i.e. the phosphorus atom of the  $\alpha$ -phosphate group of CTP and the O3' atom in the RNA primer terminus (Fig. S2b) fell  $2 \times / 18 \times$  below the 2.9/2.95 Å threshold (Fig. 3—Graph A10).

### 2dCTP: Figs. 1b, 4—Graph B01–B10

2dCTP started in the A-RNA-like conformation with the deoxyribose in the **C3'-endo** conformation (Fig. 4—Graph B2). **C2'-endo** was predominant after elapsing of about 250 ns. However, up to the end of the MD simulation repuckerings into the **C3'-endo** conformer lasting for several tens of ns were observed. It means that the minor **C3'-endo** conformers of 2dCTP survived substantially longer than the minor conformers **C2'-endo** of CTP.

This bias of 2dCTP toward **C3'-endo** seems to be partly caused by hydrogen bonding of the 3'OH group (atom H3T—Fig. 1a) toward the  $\beta$ -phosphate group of 2dCTP (atom O3—Fig. 1a)—compare (Fig. 4—Graph B2 with B3). This interaction was also applied in CTP (unlike all phosphonate analogs of CTP).

The O5'–C5'–C4'–O4' torsion angle (Fig. S3) was mostly in the **–gauche** conformation (Fig. 4—Graph B1) that was preferred in CTP as well (Fig. 3—Graph A1).

Overall, 2dCTP was in the same conformation as CTP within a significant part of the MD simulation (i.e. the deoxyribose in the **C3'-endo** conformation and the O5'–C5'–C4'–O4' torsion angle in the **–gauche** conformation). Despite of it, 2dCTP/CTP contacts with amino acid side chains in the NV RdRp active site were remarkably different.

Contacts between Asp247 and Ser300 residues were lost irreversibly once the deoxyribose repuckering into **C2'-endo** appeared (compare Fig. 4—Graph B5 with Graph B2). These contacts were not re-established again, apparently due to the absence of the 2'OH group, which could participate in a dynamic network of hydrogen bonds with Asp247 and Ser300.

Further, conformational transitions of the deoxyribose moiety disturbed salt bridges between Arg182 and the  $\alpha$ -phosphate group of 2dCTP (Figs. 2a, 4—Graph B8). The alternative arrangement with Arg182 bound to the oxygen atom involved in the  $\alpha$ P–O2 scissile bond, was observed just three times (Figs. 2b, 4—Graph B9)—i.e. less frequently than for CTP.



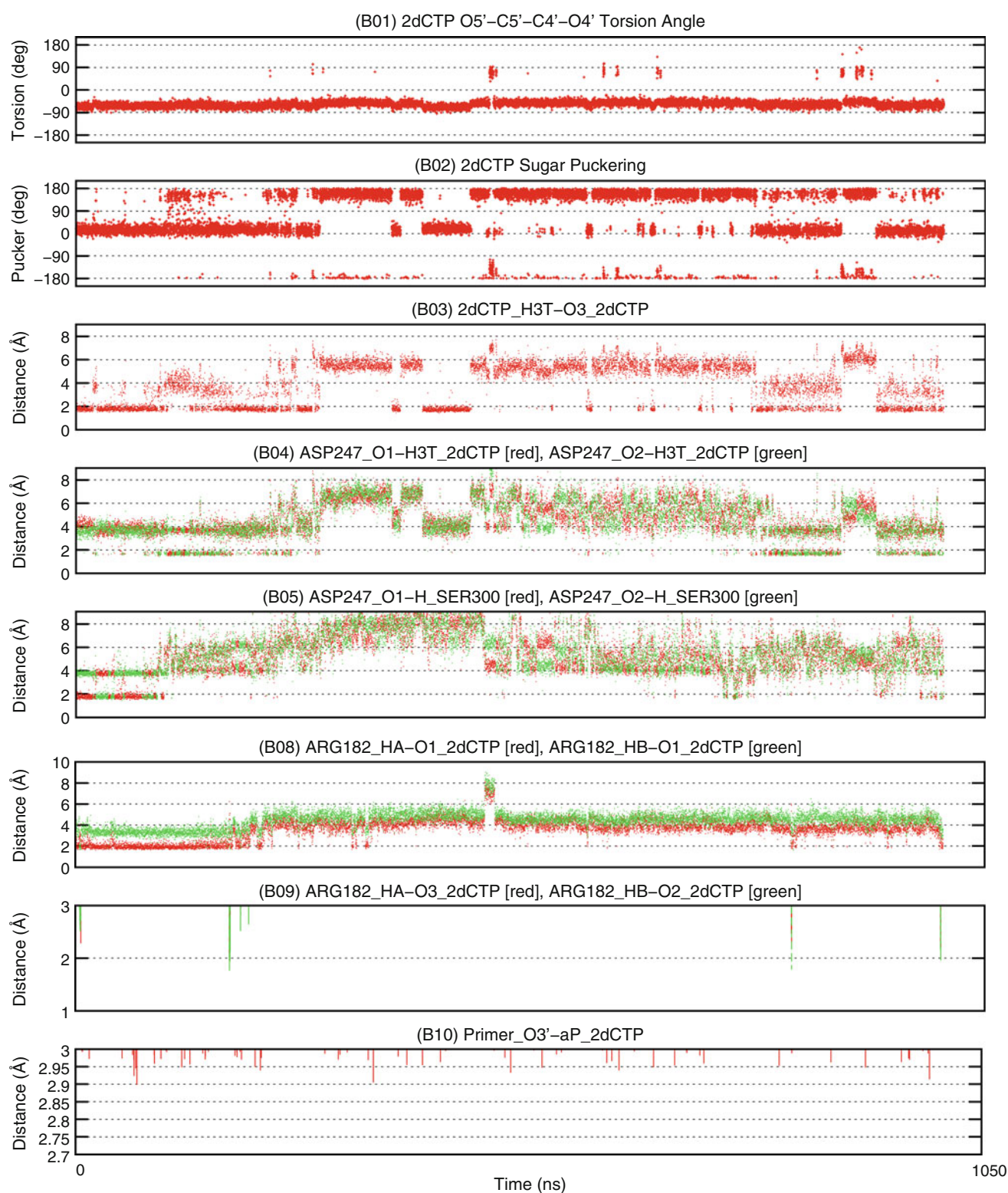


**Fig. 4** 2dCTP conformational preference and its interactions in the NV RdRp active site: **B01** 2dCTP O5'–C5'–C4'–O4' torsion angle; **B02** 2dCTP Sugar Puckering; **B03** Intramolecular hydrogen bond:

2dCTP\_3'OH– $\beta$ -phosphate\_2dCTP; **B04** Asp247–3'OH\_2dCTP; **B05** Asp247–Ser300; **B08** Arg182– $\alpha$ -phosphate\_2dCTP; **B09** Arg182– $\beta$ -phosphate\_2dCTP; **B10** Primer\_O3'– $\alpha$ -phosphate\_2dCTP

The crucial substrate–substrate distance (between the phosphorus atom in the  $\alpha$ -phosphate group of 2dCTP and the O3' atom of the RNA primer terminus) was not dropping below 2.9 Å. It fell seven times below the 2.95 Å threshold (Fig. 4—Graph B10)—i.e. less frequently than for CTP.

### coCTP: Figs. 1c, 5—Graph C01–C10

The torsion angle O5'–C5'–C4'–O4' in CTP and 2dCTP adopted the **-gauche** conformer (Fig. 3—Graph A1, Fig. 4—Graph B1). In contrast, the torsion angle C5'–O5'–C4'–O4' in coCTP (Fig. S3) preferred **+gauche** (Fig. 5—Graph C1). Therefore, it was reasonable to expect a relaxation of the coCTP positioning in the active site of NV RdRp. Surprisingly, it took hundreds of nanoseconds.

The coCTP ribose was distorted from **C3'-endo** to **C2'-exo** (Fig. 5—Graph C2). Nevertheless, short-living transitions into many different conformers were observed at the beginning of the MD simulation. Then conformational fluctuations of the C5'–O5'–C4'–O4' torsion angle from **+gauche** to **trans** appeared (Fig. 5—Graph C1). Passover of these transitions was clearly associated with a substantial rearrangement of a network of hydrogen bonds in the NV RdRp active site. It was not completed until the end of the second third of the MD simulation (Fig. 5—Graph C6).

Contacts between residues Asp247 and Ser300 disappeared after elapsing of roughly 300 ns (Fig. 5—Graph C5). Until Asp247–Ser300 contacts were lost, Ser300 served rather as a hydrogen bond acceptor from the 2'OH of coCTP. After that, Ser300 was a hydrogen bond donor for 2'OH. This contact was remarkably stable (Fig. 5—Graph C6).

Arg182 (stabilized by Glu168) was steadily in contact with the  $\alpha$ -phosphonate group of coCTP throughout the whole MD simulation (Figs. 2a, 5—Graph C08). Just one conformational transition of the Arg182 side chain toward the oxygen atom in the O2- $\alpha$ P scissile bond was observed (Fig. 5—Graph C09).

The phosphorus atom of the  $\alpha$ -phosphonate group of coCTP and the activated oxygen atom O3' of the RNA primer approached repeatedly ( $7 \times / > 40 \times$ ) below the 2.9/2.95 Å threshold (Fig. 5—Graph C10)—i.e. more a little bit more frequently than for cocCTP.

### cocCTP: Figs. 1d, 6—Graph D01–D10

The C5'–O5'–C4'–C4'' torsion angle (Fig. S3) was mostly in the **+gauche** conformation (Fig. 6—Graph D1) as in coCTP. The relaxation of the cocCTP position in the NV RdRp active site was even slower now (roughly 500 ns)

**Fig. 5** coCTP conformational preference and its interactions in the NV RdRp active site: **C01** coCTP C5'–O5'–C4'–O4' torsion angle; **C02** coCTP Sugar Puckering; **C03** Intramolecular hydrogen bond: coCTP\_3'OH– $\beta$ -phosphate\_coCTP; **C04** Asp247–3'OH\_coCTP; **C05** Asp247–Ser300; **C06** Ser300–2'OH\_coCTP; **C07** Asp247–2'OH\_coCTP; **C08** Arg182– $\alpha$ -phosphonate\_coCTP; **C09** Arg182– $\beta$ -phosphate\_coCTP; **C10** Primer\_O3'– $\alpha$ -phosphonate\_coCTP

and was made up after repuckering of the cocCTP modified sugar (the O4' atom was replaced by the  $-\text{CH}_2-$  group—Fig. S3).

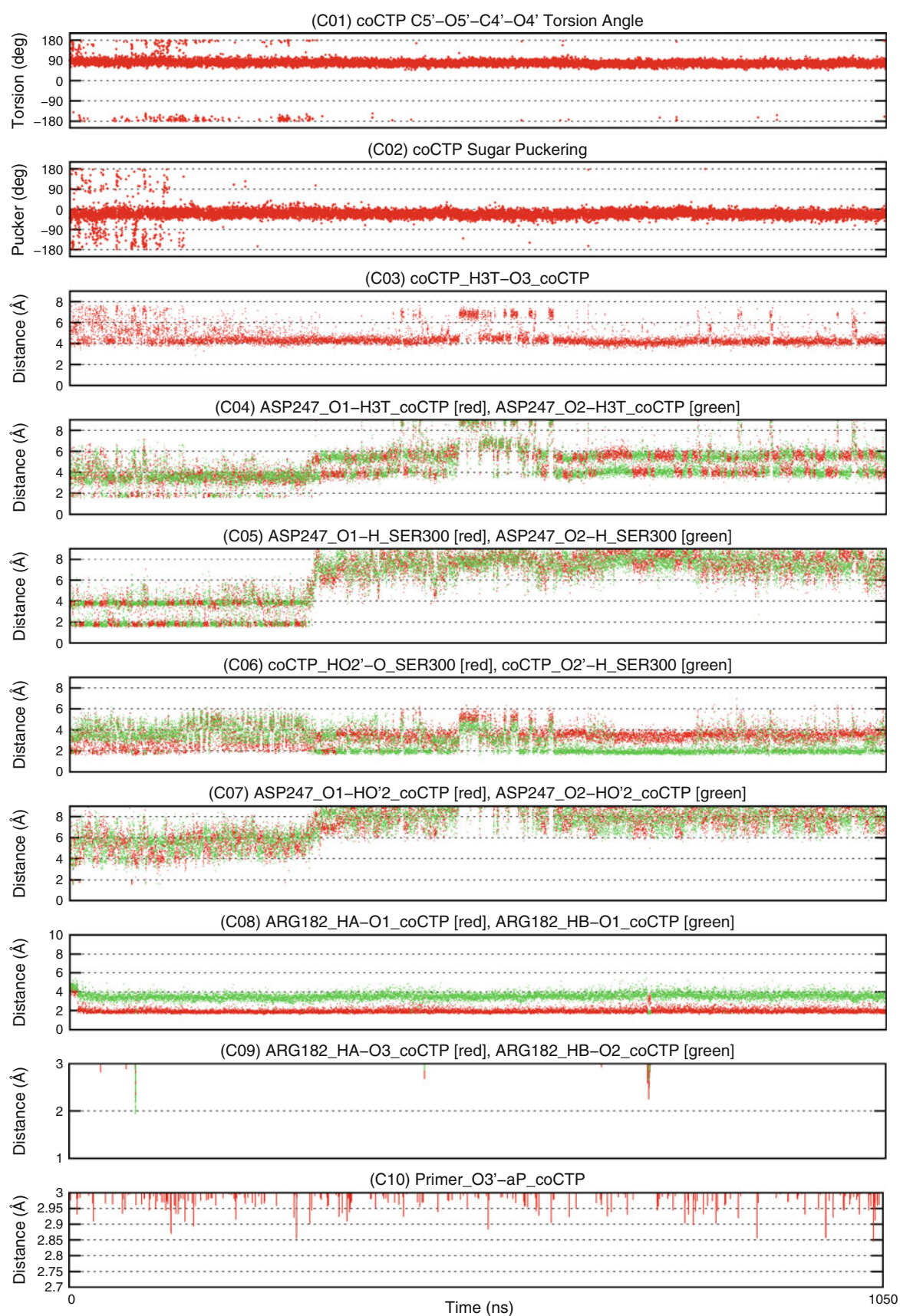
The modified sugar of cocCTP preferred the **C2'-exo** conformation almost exclusively up to 500 ns (Fig. 6—Graph D2).

While the modified sugar adopted the **C2'-exo** conformation, the Asp247–Ser300–2'OH\_cocCTP mutual contacts were remarkably stable. In fact, the Asp247–Ser300 hydrogen bonding was the most stable of all MD simulations carried out in this study (Figs. 3, 4, 5, 6—Graph A5, B5, C5, D5). It's partly due to the 3'OH group interactions with Asp247, which were considerably more stable comparing to what was observed in other MD simulations (Fig. 6—Graph D4). In CTP and 2dCTP, the 3'OH group was involved rather in the intramolecular hydrogen bonding toward the triphosphate moiety (Fig. 3—Graph A3, Fig. 4—Graph B3).

While the modified ribose have adopted the **C3'-exo** conformation, Asp247–Ser300 contacts were broken. The modified sugar of cocCTP was then in contact with the bulky side-chain of Trp246 and the 3'OH group of cocCTP was occasionally hydrogen bonded to Gln250 and Asn309. In fact, cocCTP penetrated a little bit deeper into the active site of NV RdRp beyond Asn247 in Motif A (represented as ribbon in Fig. 1).

Figure S9 shows the time evolution of the distance between the C2' atom in the 3'-terminal residue of the RNA primer (Fig. S2b) and the C1' atom in xCTPs (Fig. S2b). A significant increase of the distance is evident in the second half of the cocCTP MD simulation. This change was caused by too close contacts between the  $-\text{CH}_2-$  group (which replaced the O4' atom in the modified sugar moiety of cocCTP—Fig. S3) and a hydrogen atom bound to the C2' atom in the 3'-terminal residue of the RNA primer (Fig. S2b).

Results of preliminary calculations indicate that a steric conflict between these groups of atoms could cause that cocCTP is an inhibitor and not a chain terminator as coCTP. The topology of existing models was modified, that a bond between the  $\alpha$ -phosphate/phosphonate group of CTP (coCTP, cocCTP) and its  $\beta/\gamma$ -pyrophosphate moiety was canceled producing cytidine monophosphate (CMP) or its phosphonate analogs (coCMP, cocCMP). Instead a linkage between the terminal O3' atom of the RNA primer and the  $\alpha$ -phosphate/phosphonate group of CMP (coCMP,





cocCMP) was created. The simulated system adjusted so that it corresponds to the state immediately after the phosphoryl transfer step of the polymerase reaction (instead of the state just before the reaction) without causing a conformational change in the CMP moiety. In coCMP, the torsion angle **C5'–O5'–C4'–O4'** smoothly switched from **+gauche** to **trans** during this process. In contrast, in the case of cocCMP, the **C5'–O5'–C4'–C4''** torsion angle transition from **+gauche** to **trans** was slowed down by a steric conflict between the above mentioned groups of atoms. The question is whether this process was done, if the newly formed bond was not represented by a simple harmonic oscillator. Only future empirical valence bond (EVB) [57] and quantum mechanical/molecular mechanical (QM/MM) [58–61] calculations could resolve it.

Potentially catalytic Arg182 (stabilized by Glu168) was all the time in contact with the  $\alpha$ -phosphonate group of cocCTP (Fig. 6—Graph D8).

The distance that separates the phosphorus atom of the  $\alpha$ -phosphonate group from the O3'-end of the RNA primer drop  $5 \times / 36 \times$  below  $2.9/2.95$  Å (Fig. 6—Graph D10)—i.e. a little bit less frequently than for coCTP.

## Conclusions

Microsecond MD simulations of complexes formed between NV RdRp and its natural (CTP, 2dCTP—Fig. S3) or chemically modified (coCTP, cocCTP—Fig. S3) substrates were produced. Different conformational preferences of natural versus modified substrates were expected to appear here based on our previous experience with similarly modified dinucleotides and oligonucleotides. NMR evidences [48] that while the O5'–C5'–C4'–O4' torsion angle of natural dinucleotides prefers the **-gauche** conformer, the **C5'–O5'–C4'–O4'** torsion angle of phosphonate dinucleotides adopts the **+gauche** rotamer. Indeed, the O5' oxygen atom of CTP and 2dCTP was located above the ribose ring (Fig. 1a,b), whereas the C5' atom of coCTP and cocCTP analogs was directed outside this ring (Fig. 1c,d). The same conformational preference was seen in the crystal structure of a similar isosteric phosphonate analogue GS-9148 in the active site of HIV RT (PDB id: 3kk1 [49]). Further, we looked at how xCTPs interact with the side chains of amino acids whose mutation significantly decreases the catalytic efficiency of RdRp (i.e. Arg183 [52] interacting with the triphosphate moiety and Asp247 [50, 51] involved together with Ser300 and Asn309 in recognition of the 2'OH group). Major differences in conformational preferences and binding of the natural substrates (CTP, 2dCTP) and of their isosteric phosphonate

**Fig. 6** cocCTP conformational preference and its interactions in the NV RdRp active site: **D01** cocCTP **C5'–O5'–C4'–C4''** torsion angle; **D02** cocCTP Sugar Puckering; **D03** Intramolecular hydrogen bond: cocCTP\_3'OH– $\beta$ -phosphate\_cocCTP; **D04** Asp247–3'OH\_cocCTP; **D05** Asp247–Ser300; **D06** Ser300–2'OH\_cocCTP; **D07** Asp247–2'OH\_cocCTP; **D08** Arg182– $\alpha$ -phosphonate\_cocCTP; **D09** Arg182– $\beta$ -phosphate\_cocCTP; **D10** Primer\_O3'– $\alpha$ -phosphonate\_cocCTP

analog (coCTP, cocCTP) into the active site of NV RdRp are depicted on Fig. 1.

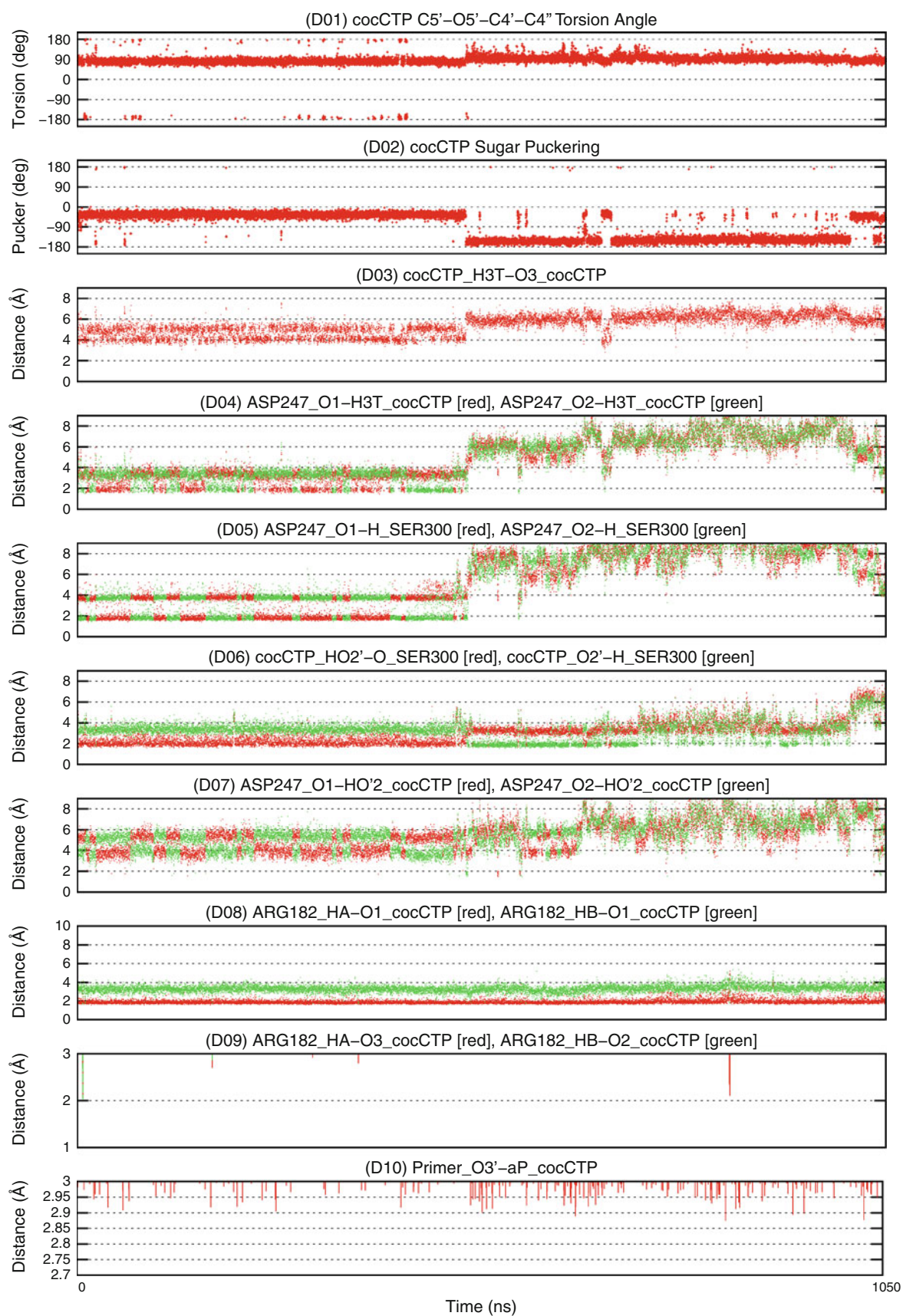
The CTP ribose was in the **C3'-endo** conformation and the O5'–C5'–C4'–O4' torsion angle adopted the **-gauche** conformer. The Asp247–Ser300–2'OH\_CTP hydrogen bond network (known from crystal structures [3, 4], Fig. 1a) was vital. Nevertheless, all imaginable combinations of hydrogen bond donors and acceptors were realized in the flow of time. About once every 100 ns, a substantial conformational change of the Arg182 side chain was observed. Arg182 then interacted with the  $\beta$ -phosphate instead of the  $\alpha$ -phosphate group of CTP (compare Fig. 2a, b).

The 2dCTP deoxyribose preferred the **C2'-endo** conformation. However, **C3'-endo** was populated too—partly due to the intramolecular bonding between the 3'OH and  $\beta$ -phosphate group of 2dCTP (also observed in CTP—but not in CTP analogs). Contacts between Asp247 and Ser300 side chains were irreversibly interrupted (recall that 2dCTP lacks the 2'OH hydroxyl group that could participate in mutual contacts). The 3'OH group of 2dCTP occasionally interacted with the side chain of Asp247 (Fig. 1b). Further, the Arg182 side chain lost contacts with the triphosphate moiety of 2dCTP. It clearly shows that binding of proper CTP and undesired 2dCTP building blocks into the NV RdRp active site differs in many aspects.

In coCTP, the **C5'–O5'–C4'–O4'** torsion angle preferred the **+gauche** rotamer from the very beginning of the MD simulation (Fig. 1c). The ribose was in the **C3'-endo/C2'-exo** conformation. Yet positional relaxations of coCTP in the NV RdRp active site took place on the timescale of hundreds of ns. After their completion, the 2'OH group of coCTP was in close contacts with Ser300 and also near to Asn309. Arg178 formed salt bridges with the  $\alpha$ -phosphonate group of coCTP during the whole MD simulation.

In cocCTP, the **C5'–O5'–C4'–C4''** torsion angle preferred again the **+gauche** rotamer from the very beginning of the MD simulation. Initially, the modified sugar of cocCTP was in the **C2'-exo** conformation (as in coCTP). At that time the Asp247–Ser300–2'OH\_cocCTP hydrogen-bond network was extremely stable, since the 3'OH group of cocCTP was involved too. After of about 500 ns, the modified sugar moiety repuckered to **C3'-exo**. cocCTP consequently penetrated a little bit deeper (Fig. S9) into the active site of NV RdRp beyond Asn 247 in Motif A (represented as ribbon in Fig. 1d). The modified sugar of cocCTP was then in contact with the bulky side-chain of





Trp246 and the 3'OH group of cocCTP was occasionally hydrogen bonded to Gln250 and Asn309. This conformational transition was caused by too close contacts between the -CH<sub>2</sub>- group of atoms (which replaced the O4' atom in the modified sugar moiety of cocCTP—Fig. S3) and a hydrogen atom bound to the C2' atom in the 3'-terminal residue of the RNA primer (Fig. S2b). Results of preliminary calculations indicate that a steric conflict between these atoms could cause that cocCTP is an inhibitor and not a chain terminator as coCTP.

Summarized, the **+gauche** conformer of the C5'–O5'–C4'–O4' and C5'–O5'–C4'–C4'' torsion angles was preferred in coCTP and cocCTP from the beginning of MD simulations (as expected based on NMR [48] and X-ray [49] studies of closely related systems). Surprisingly, the full positional relaxation of xCTP analogs in the NV RdRp active site took hundreds of nanoseconds. In hindsight, the microsecond length of MD trajectories appears to be rather a necessary minimum.

In here presented MD simulations, the NV RdRp active site in a state just before the phosphoryl-transfer step was studied. To address the question what is happening before and after this moment, different computational approaches will be required in which, however, conformers from current MD simulations will serve as starting points. Without extensive sampling of conformational space carried out in this study, those subsequent calculations were based on misleading initial structures especially in the case of CTP analogs.

Future EVB [57] and QM/MM [58–61] calculations will deal with the phosphoryl transfer step. In this case, snapshots from current MD simulations, when the O3'– $\alpha$ P substrate–substrate distance was minimal, will be used. Further, here presented MD simulations raised several questions, which evidently can be addressed only by QM/MM calculations. In the case of natural NTPs, Arg182 is a catalytic residue [52]. Nevertheless, which from the alternative conformers of Arg182 observed here is responsible for it? Could contacts of Arg182 with the  $\alpha$ -phosphonate group of coCTP and cocCTP rather hinder the phosphoryl transfer step?

A complete process of a ligand binding into protein active sites was studied recently by atomic MD simulations [43]. For polymerases, analogous calculations are unfeasible using conventional hardware resources especially due to the strong binding of magnesium ions to ligands resulting in a very slow sampling of configurational space in MD simulations. Here presented MD trajectories starting with fully formed coordination shells of magnesium ions show that merely minor positional relaxations of xCTP analogues in the NV RdRp active site can take hundreds of nanoseconds. Anyway, snapshots from here presented MD trajectories can serve as starting points for MD

simulations showing how CTP (and its analogues) leaves the NV RdRp active site, which is moving from close to open state. This reverse process can be effectively accelerated by means of metadynamics [62, 63], replica exchange molecular dynamics [64, 65] or steered molecular dynamics [66, 67].

**Acknowledgments** This work was supported by the Grant Agency of the Czech Republic (202/09/0193). The access to computing and storage facilities owned by parties and projects contributing to the National Grid Infrastructure MetaCentrum, provided under the programme “Projects of Large Infrastructure for Research, Development, and Innovations” (LM2010005) is highly acknowledged.

## References

1. Sofia MJ, Chang W, Furman PA, Mosley RT, Ross BS (2012) Nucleoside, nucleotide, and non-nucleoside inhibitors of hepatitis C virus NS5B RNA-dependent RNA-polymerase. *J Med Chem* 55:2481–2531
2. De Francesco R, Migliaccio G (2005) Challenges and successes in developing new therapies for hepatitis C. *Nature* 436:953–960
3. Zamyatkin DF, Pirra F, Alonso JM, Harki DA, Peterson BR, Grochulski P, Ng KK-S (2008) Structural insights into mechanisms of catalysis and inhibition in norwalk virus polymerase. *J Biol Chem* 283:7705–7712
4. Zamyatkin DF, Parra F, Machín A, Grochulski P, Ng KK-S (2009) Binding of 2'-amino-2'-deoxycytidine-5'-triphosphate to norovirus polymerase induces rearrangement of the active site. *J Mol Biol* 390:10–16
5. Paeshuyse J, Vliegen I, Coelmont L, Leyssen P, Tabarrini O, Herdewijn P, Mittendorfer H, Easmon J, Cecchetti V, Bartenschlager R, Puerstinger G, Neyts J (2008) Comparative in vitro anti-hepatitis c virus activities of selected series of polymerase, protease, and helicase inhibitors. *Antimicrob Agents Chemother* 52(9):3433–3437
6. Bressanelli S, Tomei L, Rey FA, De Francesco R (2002) Structural analysis of the hepatitis C virus RNA polymerase in complex with ribonucleotides. *J Virol* 76:3482–3492
7. Ng KK, Pendas-Franco N, Rojo J, Boga JA, Machin A, Alonso JM, Parra F (2004) Crystal structure of norwalk virus polymerase reveals the carboxyl terminus in the active site cleft. *J Biol Chem* 279:16638–16645
8. Gong P, Peersen OB (2010) Structural basis for active site closure by the poliovirus RNA-dependent RNA polymerase. *Proc Natl Acad Sci* 107:22505–22510
9. Arnold JJ, Gohara DW, Cameron CE (2004) Poliovirus RNA-dependent RNA polymerase (3Dpol): pre-steady-state kinetic analysis of ribonucleotide incorporation in the presence of Mn<sup>2+</sup>. *Biochemistry* 43:5138–5148
10. Huang HF, Chopra R, Verdine GL, Harrison SC (1998) Structure of a covalently trapped catalytic complex of HIV-1 reverse transcriptase: implications for drug resistance. *Science* 282:1669–1675
11. Migliaccio G, Tomassini JE, Carroll SS, Tomei L, Altamura S, Bhat B, Bartholomew L, Bosserman MR, Ceccacci A, Colwell LF, Cortese R, De Francesco R, Eldrup AB, Getty KL, Hou XS, LaFemina RL, Ludmerer SW, MacCoss M, McMasters DR, Stahlhut MW, Olsen DB, Hazuda DJ, Flores OA (2003) Characterization of resistance to non-obligate chain-terminating ribonucleoside analogs that inhibit hepatitis C virus replication in vitro. *J Biol Chem* 278(49):49164–49170

12. Zlatev I, Dutartre H, Barvik I, Neyts J, Canard B, Vasseur JJ, Alvarez K, Morvan F (2008) Phosphoramidate dinucleosides as hepatitis C virus polymerase inhibitors. *J Med Chem* 51(18): 5745–5757
13. Priet S, Zlatev I, Barvik I Jr, Geerts K, Leyssen P, Neyts J, Dutartre H, Canard B, Vasseur JJ, Morvan F, Alvarez K (2010) 3'-Deoxy phosphoramidate dinucleosides as improved inhibitors of hepatitis C virus subgenomic replicon and NS5B polymerase activity. *J Med Chem* 53:6608–6617
14. Wales DL, Schooley RT, Kaihara KA, Beadle JR, Hostetler KY (2008) Anti-hepatitis C virus replicon activity of alkoxyalkyl esters of (S)-HPMPA and other acyclic nucleoside phosphonates. *Antiviral Res* 78(2):A21
15. Koh Y, Shim JH, Wu JZ, Zhong W, Hong Z, Girardet JL (2005) Design, synthesis, and antiviral activity of adenosine 5'-phosphonate analogues as chain terminators against hepatitis C virus. *J Med Chem* 48:2867–2875
16. Sheridan C (2012) Calamitous HCV trial casts shadow over nucleoside drugs. *Nature Biotechnol* 30:1015–1016
17. Radhakrishnan R, Schlick T (2006) Correct and incorrect nucleotide incorporation pathways in DNA polymerase beta. *Biochem Biophys Res Commun* 24:521–529
18. Radhakrishnan R, Schlick T (2005) Fidelity discrimination in DNA polymerase beta: differing closing profiles for a mismatched (G:A) versus matched (G:C) base pair. *J Am Chem Soc* 127:13245–13253
19. Radhakrishnan R, Schlick T (2005) Orchestration of cooperative events in DNA synthesis and repair mechanism unraveled by transition path sampling of DNA polymerase beta's closing. *Proc Natl Acad Sci* 101:5970–5975
20. Lin P, Pedersen LC, Batra VK, Beard WA, Wilson SH, Pedersen LG (2006) Energy analysis of chemistry for correct insertion by DNA polymerase beta. *Proc Natl Acad Sci* 103:13294–13299
21. Lin P, Batra VK, Pedersen LC, Beard WA, Wilson SH, Pedersen LG (2008) Incorrect nucleotide insertion at the active site of a G:A mismatch catalyzed by DNA polymerase beta. *Proc Natl Acad Sci* 105:5670–5674
22. Wang L, Yu X, Hu P, Broyde S, Zhang Y (2007) A water-mediated and substrate-assisted catalytic mechanism for *Sulfolobus solfataricus* DNA polymerase IV. *J Am Chem Soc* 129: 4731–4737
23. Sucato CA, Upton TG, Kashemirov BA, Batra VK, Martinek V, Xiang Y, Beard WA, Pedersen LC, Wilson SH, McKenna CE, Florian J, Warshel A, Goodman MF (2007) Modifying the beta, gamma leaving-group bridging oxygen alters nucleotide incorporation efficiency, fidelity and the catalytic mechanism of DNA polymerase beta. *Biochemistry* 46:461–471
24. Oelschlaeger P, Klahn M, Beard WA, Wilson SH, Warshel A (2007) Magnesium-cationic dummy atom molecules enhance representation of DNA polymerase beta in molecular dynamics simulations: improved accuracy in studies of structural features and mutational effects. *J Mol Biol* 366:687–701
25. Jorgensen WL, Chandrasekhar J, Madura J, Impey RW, Klein ML (1983) Comparison of simple potential functions for simulating liquid water. *J Chem Phys* 79:926–935
26. Pearlman DA, Case DA, Caldwell JW, Ross WR, Cheatham TE, DeBolt S, Ferguson D, Seibel G, Kollman P (1995) AMBER, a package of computer programs for applying molecular mechanics, normal mode analysis, molecular dynamics and free energy calculations to simulate the structural and energetic properties of molecules. *Comput Phys Commun* 91:1–41
27. Cornell WD, Cieplak P, Bayly CI, Gould IR, Merz KM, Ferguson DM, Spellmeyer DC, Fox T, Caldwell JW, Kollman PA (1995) A 2nd generation force-field for the simulation of proteins, nucleic acids, and organic-molecules. *J Am Chem Soc* 117:5179–5197
28. Perez A, Marchan I, Svozil D, Sponer J, Cheatham TE III, Laughton ChA, Orozco M (2007) Refinement of the AMBER force field for nucleic acids: improving the description of alpha/gamma conformers. *Biophys J* 92:3817–3829
29. Dal Peraro M, Spiegel K, Lamoureux G, De Vivo M, De Grado WF, Klein ML (2007) Modeling the charge distribution at metal sites in proteins for molecular dynamics simulations. *J Struct Biol* 157:444–453
30. Xiang Y, Oelschlaeger P, Florian J, Goodman MF, Warshel A (2006) Simulating the effect of DNA polymerase mutations on transition-state energetics and fidelity: evaluating amino acid group contribution and allosteric coupling for ionized residues in human pol beta. *Biochemistry* 45:7036–7048
31. Florian J, Goodman MF, Warshel A (2003) Computer simulation of the chemical catalysis of DNA polymerases: discriminating between alternative nucleotide insertion mechanisms for T7 DNA polymerase. *J Am Chem Soc* 125:8163–8177
32. Aquist J (1990) Ion-water interaction potentials derived from free energy perturbation simulations. *J Phys Chem* 94:8021–8024
33. Sgrignani J, Magistrato A (2012) The structural role of Mg<sup>2+</sup> + ions in a class I RNA polymerase ribozyme: a molecular simulation study. *J Phys Chem B* 116:2259–2268
34. Phillips JC, Braun R, Wang W, Gumbart J, Tajkhorshid E, Villa E, Chipot C, Skeel RD, Kale L, Schulten K (2005) Scalable molecular dynamics with NAMD. *J Comput Chem* 26:1781–1802
35. Cheatham TE, Miller JL, Fox T, Darden TA, Kollman PA (1994) Molecular dynamics simulations on solvated biomolecular systems: the particle mesh Ewald method leads to stable trajectories of DNA, RNA, and proteins. *J Am Chem Soc* 117:4193–4194
36. Ryckaert JP, Ciccotti G, Berendsen HJC (1977) Numerical integration of the cartesian equations of motion of a system with constraints: molecular dynamics of n-alkanes. *J Comput Phys* 23:327–341
37. Harvey MJ, Giupponi G, De Fabritiis G (2009) ACEMD: accelerating biomolecular dynamics in the microsecond time scale. *J Chem Theory Comput* 5:1632–1639
38. ACEMD <http://www.acellera.com/>
39. Andersen HC (1983) RATTLE: a “velocity” version of the SHAKE algorithm for molecular dynamics calculations. *J Comput Phys* 52:24–34
40. Lambrakos SG, Boris JP, Oran ES, Chandrasekhar I, Nagumo M (1989) A modified SHAKE algorithm for maintaining rigid bonds in molecular dynamics simulations of large molecules. *J Comput Phys* 85:473–486
41. Giorgino T, Gianni de Fabritiis (2011) A high-throughput steered molecular dynamics study on the free energy profile of ion permeation through gramicidin A. *J Chem Theor Comput* 7:1943–1950
42. Selent M, Sanz F, Pastor M, De Fabritiis G (2010) Induced effects of sodium ions on dopaminergic G-protein coupled receptors. *PLOS Comput Biol* 6:e1000884
43. Buch I, Giorgino T, De Fabritiis G (2011) Complete reconstruction of an enzyme-inhibitor binding process by molecular dynamics simulations. *Proc Natl Acad Sci* 108:10184–10189
44. Feenstra KA, Hess B, Berendsen HJC (1999) Improving efficiency of large time-scale molecular dynamics simulations of hydrogen-rich systems. *J Comput Chem* 20:786–798
45. Humphrey W, Dalke A, Schulten K (1996) VMD—visual molecular dynamics. *J Mol Graph* 14:33–38
46. Pettersen EF, Goddard TD, Huang CC, Couch GS, Greenblatt DM, Meng EC, Ferrin TE (2004) UCSF chimera—a visualization system for exploratory research and analysis. *J Comput Chem* 25:1605–1612
47. Lavery R, Moakher M, Maddocks JH, Petkeviciute D, Zakrzewska K (2009) Conformational analysis of nucleic acids revisited: curves+. *Nucleic Acids Res* 37:5917–5929

48. Točík Z, Buděšínský M, Barvík I Jr, Rosenberg I (2009) Conformational evaluation of labeled C3'-O-P-(13)CH(2)-O-C4'' phosphonate internucleotide linkage, a phosphodiester isostere. *Biopolymers* 91:514–529
49. Lansdon EB, Samuel D, Lagpacan L, Brendla KM, White KL, Hung M, Liu X, Boojamra CG, Mackman RL, Cihlar T, Ray AS, McGrath ME, Swaminathan S (2010) Visualizing the molecular interactions of a nucleotide analog, GS-9148, with HIV-1 reverse transcriptase-DNA complex. *J Mol Biol* 397:967–978
50. Arnold JJ, Cameron CE (2004) Poliovirus RNA-dependent RNA polymerase (3Dpol): pre-steady-state kinetic analysis of ribonucleotide incorporation in the presence of  $Mg^{2+}$ . *Biochemistry* 43:5126–5137
51. Gohara DW, Crotty S, Arnold JJ, Yoder JD, Andino R, Cameron CE (2000) Poliovirus RNA-dependent RNA polymerase (3Dpol). *J Biol Chem* 275:25523–25532
52. Ranjith-Kumar CT, Sarisky RT, Gutshall L, Thomson M, Kao CC (2004) De Novo initiation pocket mutations have multiple effects on hepatitis C virus RNA-dependent RNA polymerase activities. *J Virol* 78:12207–12217
53. Sarafianos SG, Pandey VN, Kaushik N, Modak MJ (1995) Site-directed mutagenesis of arginine 72 of HIV-1 reverse transcriptase. *J Biol Chem* 270:19729–19735
54. Glennon TM, Villa J, Warshel A (2000) How does GAP catalyze the GTPase reaction of Ras?: a computer simulation study. *Biochemistry* 39:9641–9651
55. te Heesen H, Gerwert K, Schlitter J (2007) Role of the arginine finger in Ras. RasGAP revealed by QM/MM calculations. *FEBS Lett* 581:5677–5684
56. Oldham WM, Hamm HE (2006) Structural basis of function in heterotrimeric G proteins. *Q Rev Biophys* 39:117–166
57. Kamerlin SCL, Warshel A (2011) The empirical valence bond model: theory and applications. *Wiley Interdiscip Rev Comput Mol Sci* 1:30–45
58. Sgrignani J, Magistrato A (2013) First-principles modeling of biological systems and structure-based drug-design. *Current Comput Aided Drug Design* 9:15–34
59. Senn HM, Thiel W (2009) QM/MM methods for biomolecular systems. *Angew Chem Int Ed* 48:1198–1229
60. Groenhof G (2013) Introduction to QM/MM simulations. *Methods Mol Biol* 924:43–66
61. Vreven T, Byun KS, Komaromi I, Dapprich S, Montgomery JA Jr, Morokuma K, Frisch MJ (2006) Combining quantum mechanics methods with molecular mechanics methods in ONIOM. *J Chem Theory Comput* 2:815–826
62. Laio A, Gervasio FL (2008) Metadynamics: a method to simulate rare events and reconstruct the free energy in biophysics, chemistry and material science. *Rep Progr Phys* 71:126601
63. Gervasio FL, Laio A, Parrinello M (2005) Flexible docking in solution using metadynamics. *J Am Chem Soc* 127:2600–2607
64. Grater F, de Groot BL, Jiang H, Grubmuller H (2006) Ligand-release pathways in the pheromone-binding protein of bombyx mori. *Structure* 14:1567–1576
65. Sugita Y, Okamoto Y (1999) Replica-exchange molecular dynamics method for protein folding. *Chem Phys Lett* 314:141–151
66. Li MS, Mai BK (2012) Steered molecular dynamics—a promising tool for drug design. *Curr Bioinform* 7:342–351
67. Grubmuller H, Heymann B, Tavan P (1996) Ligand binding: molecular mechanics calculation of the streptavidin-biotin rupture force. *Science* 271:997–999